Computational Analysis of the Failure Mechanisms of a Laminated Composite in Double-Edge Notch Compression Configuration

Alex Faupel[a], Caglar Oskay[a,2]

[a]Department of Civil and Environmental Engineering, Vanderbilt University, Nashville, 37235, TN, USA

ARTICLE INFO

Keywords:
C. Computational modelling
A. Laminates
C. Damage mechanics
C. Finite element analysis (FEA)

ABSTRACT

This manuscript presents a combined experimental-computational investigation of the compression failure response of laminated composites in double-edge notch compression (DENC) configuration. Analysis of in-situ and post-test DENC experiment results indicates the presence of multiple failure mechanisms, including ply splitting, delamination, and compression kink bands. In order to characterize the onset, growth, and interplay of the critical and subcritical damage mechanisms, a multiscale progressive damage analysis approach is implemented. A nonlocal multiscale damage model explicitly tracks the intraply failure mechanisms that lead to the formation and propagation of kink bands in the specimen. A cohesive zone model is used to track initiation and progression of ply splitting in the specimen. The splitting model was implemented using implicit finite element simulations and deployed with a pre-crack insertion technique to reduce simulation time while preserving prediction accuracy. Model parameters are calibrated based on available calibration data and measurements. The effects of split location and growth characteristics on model predictions are studied. The computational model along with a suite of experiments were employed to study the formation, growth and interactions of damage mechanisms in the composite specimens subjected to compression loading. The onset of matrix damage is not clear from the experimental images but the model predicts early onset around the onset time of splits which greatly reduce the stress concentration at the notches. Analysis of acoustic emission energy experimental data indicate that observable compression failure mechanisms are not causing nonlinearity consistently exhibited in the experiment responses. Simulation results demonstrate the capability of the multiscale modeling approach to predict critical kink bands and sub-critical matrix cracking and splitting in the DENC specimens while reducing computational cost compared to a direct numerical simulation of fibers and matrix.

1. Introduction

A critical weakness of laminated carbon-fiber reinforced polymer (CFRP) composites is their longitudinal compression strength. Results from experiments on unidirectional specimens report as low as 60% of the strength of the same material under tension loading [24, 78, 84]. Computational prediction of the behavior and associated failure mechanisms is therefore essential for effective design of composite structures operating under compressive loading. The behavior is complicated due to the presence of multiple failure mechanisms which include kink banding, splitting, delamination, fiber cracking, fiber-matrix debonding, and matrix cracking [36, 58, 66, 67, 71, 72, 81], some of which interact during the loading process. Progressive damage analysis models that incorporate the appropriate mechanisms at multiple scales and that capture the interactions between these mechanisms (thereby going beyond the capabilities of traditional approaches, such as strength-based failure models) are therefore needed.

Several computational damage and failure analysis techniques have been employed to model failure mechanisms associated with the compression response of CFRP composites. Among the compression failure mechanisms, kink bands have been shown to strongly influence the compression strength of composites [43, 49, 63, 66, 72, 82]. Kink banding is an instability phenomenon [2, 19, 34, 43, 49, 50] and numerical studies suggest a strong link between fiber misalignment, mechanical properties of the constituent materials, and the resulting compression strength [33, 80, 86]. Modeling approaches for kink band failure span direct numerical simulations [14, 51, 86] that resolve the composite constituents at the mesoscale, continuum damage models that track fiber rotation and incorporate shear nonlinearity at the mesoscale [10, 11], multiscale modeling that concurrently evaluates failure processes in resolved materials microstructures across the macroscale domain [33], and models based on macroscale failure criteria by including effects of shear nonlinearity and pressure [57] or critical fiber misalignments [20, 83]. Other mechanisms (i.e., splitting, delamination, matrix cracking, and fiber-matrix debonding) are not unique to compression loading and are typically observed under other loading conditions as well [52, 61]. Fracture mechanics-based approaches such as cohesive zone modeling (CZM) [10, 29, 51, 74] and extended finite element method [27, 38], continuum damage mechanics [21, 29, 74], multiscale methods such as the eigenstrain based homogenization method [16, 17, 25, 26], multiscale discrete damage theory [55, 69, 70], and criterion-based failure models [20, 87], among others have been employed to study the aforementioned failure mechanisms. Fiber fracture is a consequence of the bending experienced in microbuckling

*Corresponding author
caglar.oskay@vanderbilt.edu (C. Oskay)
ORCID(s):
1

and/or kink band formation [43] and has been included using strength [7, 20] or curvature criteria [33].

Recent experimental studies shed some light into the compression failure interactions in laminated CFRP composites. Physical testing of compression specimens provided some understanding of the order of occurrence of failure mechanisms in composite laminates of varying layups and configurations. The ultimate failure is typically induced by the propagation of the dominant kink band across a 0 degree lamina [9, 12, 23, 73]. Prominent splitting is also consistently observed prior to failure in notched specimens at the notches and within multiple laminae of different directions [9, 12, 23]. Matrix cracking and delaminations are present and observed connecting to kink bands [9, 12, 23].

Recent computational investigations provide information on the interactions between the failure mechanisms throughout the loading process [12, 15, 60]. Prabhakar and Waas [60] investigated several unnotched laminate layup configurations. The onset of kink bands was predicted just prior to the ultimate load, whereas delaminations were predicted to fully form after kink band onset. This study also showed that increasing interlaminar shear strength results in delayed kink band initiation and increased laminate compression strength, pointing to interaction between interlaminar damage state and kink band initiation. Bishara et al. [15] investigated the progression of failure in unnotched $[+45/90/-45/0]_{2S}$ specimens. Delaminations were predicted to fully form early in the process at 90-45 degree ply interfaces near the edges of the specimen (at approximately 77% of the ultimate load). Kink bands initiated immediately prior to the ultimate load away from these delaminations. Matrix cracking in the 45 and 90 degree plies were also predicted post-ultimate load. Additional delaminations were predicted at the 0-90 and 0-45 degree ply interfaces connecting to the ends of the formed kink band. Bergan et al. [12] studied the progression of damage in 3 different open-hole layups which exhibited 3 different effective stiffnesses. Initial splitting and matrix cracking are predicted around 75% of the respective ultimate load in all specimens, followed by kink band initiation around 97-99%. The early onset damage features exhibit differences in initial size and growth. Long initial splits were predicted in the stiffest laminate and are accompanied by a small amount of delamination prior to failure. In contrast, delaminations were predicted with size matching short splits prior to ultimate load in the least stiff laminate. The results of this investigation show variation of failure mechanism initiation time, initial size, and growth among specimens consisting of the same material. Other investigations of laminate specimens with rectangular central hole and asymmetric layup indicate failure mechanism initiation after the onset of buckling [30–32]). The aforementioned studies point to uncertainties in compression failure mechanism interactions and how these interactions influence overall compressive performance.

A recent experimental investigation performed on double-edge notched CFRP specimens provide additional insight into the progressive damage growth under quasi-static compressive loading [23]. The geometry and layup of the specimen resulted in stable damage progression which enabled detailed experimental characterization of failure onset and growth as a function of load amplitude. The work presented in this manuscript employs a multiscale computational model to study the onset, growth, and interplay of the failure mechanisms observed in the double-edge notched compression (DENC) experiments. A nonlocal multiscale model originally proposed in Ref. [33] is generalized to study laminated kink band formation and propagation. A CZM-based model is incorporated to study the effect of splitting on the compression performance of the DENC samples. The kink band and splitting models were calibrated based on a suite of experimental data and image analysis. DENC specimens were simulated with the calibrated model and a detailed analysis of how progressive splitting and kink band failure interacts to culminate in specimen failure is performed based on computational and experimental evidence. A unique contribution of this work is that it compares the predicted onset and progression of compression failure mechanisms to experimental data and images generated from specimens subjected to sub-critical loads.

2. Methods

2.1. Experimental

Experiments were performed at the Air Force Research Laboratory (AFRL) on CFRP laminates in a double-edge notch compression (DENC) configuration [23]. The DENC specimens were hand-laid with IM7/977-3 carbon/epoxy unidirectional pre-impregnated tape in a stacking sequence of $[0_3/+45/-45/90/0]_S$ and autoclave cured. Two notches were introduced by milling and were examined to ensure that no damage was introduced in the gage section. Tabs were bonded to both ends of the specimens using a two-part structural paste adhesive. The final specimen geometry and dimensions are shown in Fig. 1a-b. The reasons for choosing the layer arrangement and the notch geometry used in the experiments are discussed in Ref. [23]. The test procedure followed ASTM D6641 [5], where a constant displacement rate of 1.3 mm/min was applied to the gripped specimen using a combined loading compression test fixture. Load-displacement from the test machine was acquired in addition to local strains and displacements across the gage section between the notches measured using a virtual extensometer (VE) system as indicated in Fig. 1b. Both the test frame and VE data were captured at 10 Hz. Multiple other imaging techniques were employed to examine failure during testing. Optical images of the exterior surface in the gage section were captured throughout the test at 100 Hz using a digital camera. Microcomputed Tomography (μCT) scans were performed on damaged composite specimens with and without zinc-iodide dye penetrant using a Zeiss Xradia Versa 620 X-ray Microscope system equipped with a 160 kV transmission target X-ray source and a flat-panel detector. A series of optical objectives allowed multiple magnification

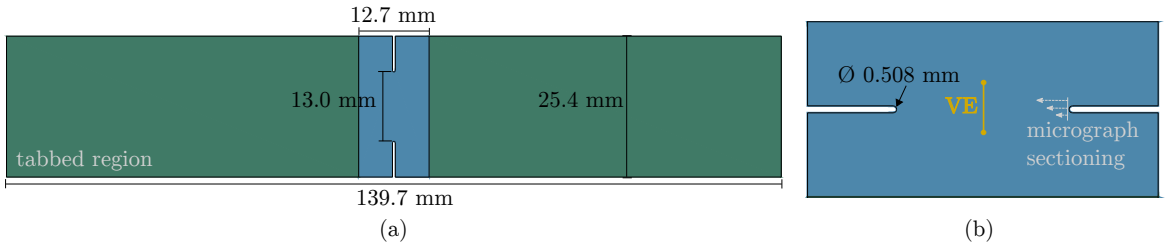

Figure 1: (a) Geometry and dimensions of the DENC test article, (b) detailed view of the gage section.

Table 1
Breakdown of experiments.

Calibration			Analysis		
Experiment	Procedure	Qty.	Experiment (stop criteria)	Procedure	Qty.
UD DENC	[5]	4	DENC (Failure)	[5]	9
V-notch shear	[3]	5	DENC (Load Interval 1)	[5]	9
DCB	[4]	5	DENC (Load Interval 2)	[5]	16
ENF	[6]	5			

levels. Micrographs were produced using a Nikon MM-60 table-top microscope, NIS-Elements D software, and a DS-Fi2 camera. Energy-event readings from acoustic emission sensors were used to define two load intervals for interrupting tests prior to ultimate load as well as an observable damage threshold. A grind/polish process was performed with these specimens and micrographs were obtained across the width of the specimens from one notch as indicated in Fig. 1b and described in [23]. No damage was detected in the test specimens when an acoustic energy jump (or event) was recorded with a value less than 10^{-13}J. The X-ray CT images provide additional detail on the internal extent of damage.

Additional property characterization experiments were performed on unidirectional 0 degree (UD) specimens. The experiments include compression loading of UD DENC specimens. Configuration, dimensions and test procedure for the UD DENC specimens are identical to the DENC specimens as shown in Fig.1, including specimen thickness. Other characterization experiments include shear loading parallel to the fiber direction of V-notch specimens, double cantilever beam (DCB), and end-notch flexure (ENF) configurations. The UD compression, DCB, and ENF tests were carried out at the AFRL. The V-notch tests were carried out at the Mechanics of Composite Materials Laboratory at Tel-Aviv University. The breakdown of experiments by calibration and analysis phase, the testing procedure followed, and the quantity of tests performed are shown in Table 1. The DENC experiments and results have been previously reported in [23]. Additional images generated during the experimental program but not included in [23] are used in the model calibration (3.1) and analysis (3.2).

2.2. Numerical Modeling

2.2.1. Multiscale Compression Kink Band Model

A reduced order multiscale model proposed in Faupel et al. [33] has been used to represent the compression kink-band failure behavior in the composite specimens. The model is based on the eigenstrain-based reduced order computational homogenization (EHM) approach which has been previously used to study progressive failure behavior of composites under a range of loading and environmental conditions [16, 17, 39, 54, 85]. The model keeps track of the failure processes associated with kink band formation at the scale of the microstructure coupled to a computational homogenization method in solving the macrostructural compression response. The evolution of nonlinear shear deformation and damage in the matrix concentrated in the kink band region are explicitly tracked. The length scale of the kink band (i.e., the kink band width) is captured by using a gradient-based nonlocal formulation. Full description and verification of the multiscale kink band model are provided in [33]. The constitutive relations for the multiscale kink band model are summarized below.

Under compression loading, the composite laminate undergoes localized instability induced by material imperfections (i.e., fiber misalignment or waviness). Kink bands form as a result of excessive deformation of the matrix and localized bending-induced fiber fracture near these regions of instabilities. The failure in the matrix is modeled using continuum damage mechanics. Upon onset of instability at the mesoscale, the fibers buckle and no longer contribute to load carrying capacity. For simplicity, explicit fiber fracture induced by local buckling is not considered in the model. The formulation described in Ref. [33] includes fiber breakage as well. Mesoscale analyses conducted with and without fiber breakage predict the same compression strength in UD specimens.

The localized large deformation behavior is captured using a co-rotational formulation, where a local coordinate system is attached to the microstructure that follows macroscopic rotation. In what follows, a superposed hat, $(\hat{\cdot})$ indicates the corresponding field expressed in local coordinates, and a superposed bar, $(\bar{\cdot})$ indicates a macroscopic quantity. At a given material point in the specimen, the macroscale Cauchy stress, $\hat{\bar{\sigma}}$, in the co-rotational frame is expressed as:

$$\hat{\bar{\sigma}} = \left[1-\omega^{(\mathrm{m})}\right]\left[\overline{\mathbf{L}}^{(\mathrm{m})} : \hat{\bar{\varepsilon}} + \overline{\mathbf{P}}^{(\mathrm{mm})} : \mu^{(\mathrm{m})}\right] + \left[\overline{\mathbf{L}}^{(\mathrm{f})} : \hat{\bar{\varepsilon}} + \overline{\mathbf{P}}^{(\mathrm{mf})} : \mu^{(\mathrm{m})}\right] \tag{1}$$

in which $\hat{\bar{\varepsilon}}$ is the macroscopic strain; $\omega^{(\mathrm{m})}$ denotes the damage state within the matrix. The scalar damage variable evolves within $0 \leq \omega^{(\mathrm{m})} < 1$ with limits $\omega^{(\mathrm{m})} = 0$ and $\omega^{(\mathrm{m})} \rightarrow 1$ respectively indicating no damage and complete loss of load carrying capacity within the matrix. $\mu^{(\mathrm{m})}$ is inelastic strain induced by the damage process within the matrix. $\overline{\mathbf{L}}^{(\cdot)}$ and $\overline{\mathbf{P}}^{(\cdot)}$ are coefficient tensors that reflect the effect of microstructural morphology on determining the macroscopic stress state ([17, 53, 68]). The kinematic equation that relates the inelastic strain coefficients to the macroscopic strain is expressed as:

$$\left[1-\omega^{(\mathrm{m})}\right]\left[\hat{\mathbf{A}}^{(\alpha\mathrm{m})} : \bar{\varepsilon} + \hat{\mathbf{B}}^{(\alpha\mathrm{mm})} : \mu^{(\mathrm{m})}\right] + \left[\hat{\mathbf{A}}^{(\alpha\mathrm{f})} : \bar{\varepsilon} + \hat{\mathbf{B}}^{(\alpha\mathrm{fm})} : \mu^{(\mathrm{m})}\right] = 0; \quad \alpha = \mathrm{m}, \mathrm{f} \tag{2}$$

in which $\hat{\mathbf{A}}^{(\cdot)}$ and $\hat{\mathbf{B}}^{(\cdot)}$ are additional coefficient tensors.

This system of equations for the model is closed by defining evolution equations for the matrix damage variable. The matrix is taken to exhibit a nonlinear hardening behavior followed by material softening. The damage behavior is described as a function of the nonlocal damage history variable, $\tilde{\kappa}^{(\mathrm{m})}$:

$$\omega^{(\mathrm{m})} = \Phi(\tilde{\kappa}^{(\mathrm{m})}); \;\; 0 \leq \Phi \leq 1 \tag{3}$$

which evolves according to the monotonic damage evolution function:

$$\Phi(\tilde{\kappa}^{(\mathrm{m})}) = \frac{\arctan(a^{(\mathrm{m})}\langle \tilde{\kappa}^{(\mathrm{m})} - \kappa_0^{(\mathrm{m})} \rangle - b^{(\mathrm{m})}) + b^{(\mathrm{m})}}{\frac{\pi}{2} + \arctan(b^{(\mathrm{m})})} \tag{4}$$

where $a^{(\mathrm{m})}$, $b^{(\mathrm{m})}$, ${\kappa_0}^{(\mathrm{m})}$ are material parameters, and the Macaulay brackets, $\langle \cdot \rangle$, are used to enforce the threshold for the onset of inelastic evolution of damage.

When not regularized, continuum damage mechanics models localize damage to a region dictated by the size of the finite elements [1, 65]. The width of the compression kink bands on the other hand are dictated by fiber properties (e.g. fiber size [86] and longitudinal modulus [34]) and matrix properties (e.g. shear nonlinearity or "ductility" [7, 50]). The model employed in this study uses a gradient based regularization scheme to consistently capture the kink band width [33]. The nonlocal equivalent damage variable is expressed using the following partial differential equation defined over the domain of the specimen parameterized by $\mathbf{x}$:

$$\tilde{\kappa}^{(\mathrm{m})}(\mathbf{x}, t) - L^2 \nabla^2 \left[\tilde{\kappa}^{(\mathrm{m})}(\mathbf{x}, t)\right] = \kappa^{(\mathrm{m})}(\mathbf{x}, t); \tag{5}$$

in which L is a length scale parameter related to the size of the kink band width, and ∇^2 denotes the Laplacian operator. $\kappa^{(\mathrm{m})}$ is defined as:

$$\kappa^{(\mathrm{m})}(\mathbf{x}, t) = \min\{\hat{\kappa}^{(\mathrm{m})}, \kappa_c\} \tag{6}$$

where κ_c denotes the value of the local damage history variable when full damage is reached (i.e., $\Phi(\hat{\kappa} = \kappa_c) \approx 1$). The local damage history variable is $\hat{\kappa}^{(\mathrm{m})}$ is defined as:

$$\hat{\kappa}^{(\mathrm{m})} = \max_{0 \leq \tau \leq t} \{\upsilon^{(\mathrm{m})}(\tau)\} \tag{7}$$

taking the value of the maximum damage equivalent strain, $\upsilon^{(\mathrm{m})}$, in the loading history. The damage equivalent strain is defined as:

$$\upsilon^{(\mathrm{m})} = \sqrt{\frac{1}{2}\hat{\epsilon}^{(\mathrm{m})} : \hat{\mathbf{L}}^{(\mathrm{m})} : \hat{\epsilon}^{(\mathrm{m})}} \tag{8}$$

which is a function of the local principal strains, $\hat{\epsilon}^{(\mathrm{m})}$, and the elastic modulus tensor, $\hat{\mathbf{L}}^{(\mathrm{m})}$, rotated to the principal directions. Neumann boundary conditions are enforced to evaluate the nonlocal equation:

$$\nabla \tilde{\kappa}^{(\mathrm{m})} \cdot \mathbf{n} = \mathbf{0} \tag{9}$$

where $\mathbf{n}$ is the unit outward normal to the domain boundaries.

A drawback of the regularization scheme employed in this study is the observed expansion of the damage region under sustained loading even after the failure is reached within the specimen (see also, e.g., Geers et al. [35] for a discussion on this type of spurious growth). We note that this is unrelated to the observation reported on the growth of the kink band width as it propagates [50, 80], as the numerical simulations exhibit widening in parts of the kink bands that have already formed as well. The spurious spread of the kink band is controlled by degrading the length scale parameter as matrix damage evolves [59]:

$$L(\mathbf{x}, t) = (c_1 w + c_2) \cdot g\left(\omega^{(\mathrm{m})}(\mathbf{x}, t)\right) \tag{10}$$

$$g = \sqrt{\frac{(1-R)\exp\left(-\eta\omega^{(\mathrm{m})}\right) + R - \exp(-\eta)}{1 - \exp(-\eta)}} \tag{11}$$

where, c_1 and c_2 are model parameters, and w is the observed kink band width; R and η are numerical constants controlling the length scale degradation.

2.2.2. *Cohesive Zone Model for Splitting*

We consider a standard CZM described in Ref. [22]. Similar CZM models have also been used in modeling splitting in CFRP composites [37, 52, 77]. The traction-separation law follows a bi-linear form using a quadratic stress damage initiation criterion and linear softening slope enforced for critical fracture energy. Mixed mode state is expressed according to the Benzeggah-Kenane relationship [8]. Evolution of the damage variable for the ply interface is as described in [22].

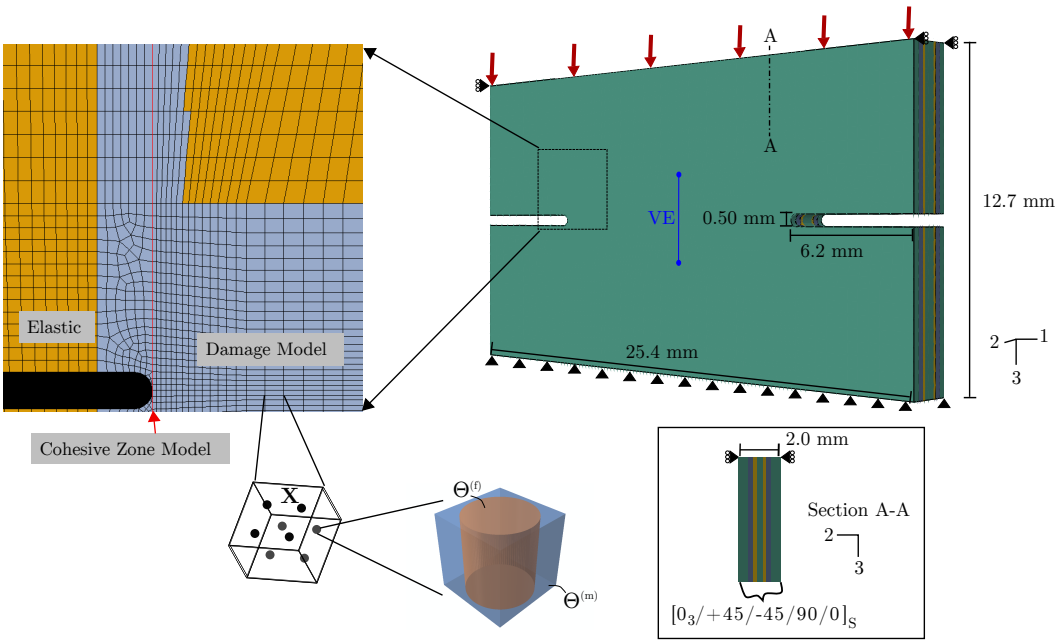

Figure 2: Analysis geometry, boundary conditions, mesh, and model assignment.

2.2.3. Implementation Details

In EHM, a nonlinear analysis and history dependent reduced order microstructure problem is concurrently evaluated with the structural scale analysis. A separate reduced order microstructure model is evaluated and tracked at each quadrature point of the macroscale discretization. Simulations are performed using commercially available implicit finite elements analysis code, Abaqus/Standard. The microstructure in the analysis is idealized as a periodic and square unit cell with two parts representing the damageable matrix and the elastic fiber. The coupled macroscopic system of equations for equilibrium and nonlocal equations is implemented through the use of coupled thermo-mechanical solver. The nonlocal equation is enforced on the 0 degree plies only, as the critical kink bands are expected to occur on 0 degree plies. Matrix damage evolution is also considered in the non-zero degree plies to predict failure by transverse cracking [17, 18]. In this case, the length scale parameter is set to a small (near zero) value since the length scale parameter is associated with the kink band width. The full implementation workflow of the kink band model is detailed in Ref. [33] and is implemented in the same manner here for the nonlocal matrix damage using a user-defined material and auxiliary data passing subroutines. In-built Abaqus capabilities are used for CZM models of splitting.

2.2.4. Simulation Setup

The geometry, discretization and the boundary conditions used in the specimen simulations are shown in Fig. 2. The domain for the analysis is constructed to match the gage section of the DENC specimen. Boundary conditions corresponding to displacement control are applied on the numerical gage section top and bottom faces which are aligned to the ends of the gripped tabs on the experiment test articles. The plies composing the laminate are modeled by dividing the geometry into equal thickness layers matching the number of plies in the layup and assigning an initial material orientation that match the ply fiber directions. Computational expense is balanced with higher resolution of the failure mechanism predictions by partitioning the ply layers into elastic and damageable regions as shown in Fig. 2 and meshed with full-integration continuum elements. The mesh size is uniform in the thickness direction, where there are two elements for every ply (i.e. 28 elements through the thickness). The mesh is structured and elements lengths vary from approximately 70 µm in between the notches to 300 µm outside of the damageable region. While damage models without regularization are typically mesh-sensitive, the compression kink band model used in this study is regularized through the gradient-based regularization scheme with the kink band width serving as the nonlocal length scale. The mesh independence of the kink band model has been demonstrated in Ref. [33].

It is well known that the initial fiber misalignment strongly affects kink band onset, and unidirectional compressive strength is very sensitive to the maximum misalignment angle [43, 80]. Selection of misalignment parameters (and the other model parameters) are described in the model calibration section below. The 0 degree plies are prescribed an initial fiber misalignment by defining the integration point orientation with the expression:

$$\psi(z) = \psi_0 \sin\left(\pi\left(\frac{z - z_0}{l} + \frac{1}{2}\right)\right) \tag{12}$$

where, z is the material coordinate in the fiber direction, z_0 is the coordinate of the notch tip in the fiber direction, ψ_0 is the maximum initial misalignment angle, and l is the half-wavelength of the function. The expression represents

a periodic form similar to the waviness in experimental observations [43, 56]. The variation in orientation corresponds to waviness in the transverse direction (1 axis in Fig. 2) and the maximum misalignment angle occurs at the notch tip. Provided that the misalignment half-wavelength is smaller than the fracture process zone, a phase shift in the assumed initial fiber misalignment (where maximum misalignment angle does not align with the notch tip) is not expected to significantly affect the onset of failure.

Splitting regions where cohesive traction can degrade are defined as longitudinal strips tangent to the notch tips in all 0 degree plies. Previous studies in the literature have also employed selectively placed splitting regions based on experimental observations when modeling edge- and center-notched specimens [37, 44, 61]. The splitting regions are meshed with full-integration continuum cohesive elements with uniform thickness of 0.1 μm and side lengths matching the ply mesh in the 2 and 3 dimensions. A linear elastic analysis indicates shear stress concentration in the plies occurring at locations near the notch end but not exactly on the notch tip. As is commonly observed with cohesive models, element lengths along the failure direction should be sufficiently small to capture the fracture process zone [28]. Furthermore, resolving the stress concentration is crucial for predicting split initiation. To address these concerns, a mesh convergence study including nominal element side lengths, h, in the 3 dimension ranging from 40 to 1 μm was performed. Convergence of the stress field is predicted with $h = 10\,\mu\text{m}$ starting at approximately 70 μm from the center of the notch (mid-height of the specimen). The final simulation element size near the notches linearly increases to $h = 160\,\mu\text{m}$ at a distance of 2 mm from the center of the notches. The 3D finite element model consists of approximately 900,000 degrees of freedom.

3. Results and Discussion

3.1. Model Calibration

The calibrated values of the kink band and local damage model parameters as well as the sources of calibration data are listed in Table 2. The starting point for the calibration of the physical parameters were the values reported in [17] and the values in [33] were used for the numerical parameters, since these studies employed similar materials. UD DENC experiments were also used in model calibration. Specifically, the unidirectional compression modulus and strength of the specimens (shown in Table 3) obtained from the UD DENC tests were used in the calibrations. In these experiments, specimens exhibited brittle failure. Splitting ahead of the notch tips early on is observed which reduced the stress concentrations near the notch tips. The ligament between the notch tips following split formation exhibits a relatively uniform stress that is equal to the load divided by the cross-sectional area between the notch tips. The longitudinal fiber elastic modulus, $E_1^{(f)}$, was calibrated using the rule of mixtures (i.e. $E_{long} = V^{(f)}E_1^{(f)} + (1 - V^{(f)})E^{(m)}$, with 65% fiber volume fraction, $V^{(\mathrm{f})}$, and E_{long} is calculated from the mean linear regression of the load-virtual extensometer data between 0.5 microstrain and 2 microstrain divided by the cross-sectional area between the notch tips.

The UD specimen strength value (calculated as the mean ultimate load of the UD DENC experiments divided by the cross-sectional area between the notch tips) was then used to calibrate the maximum fiber misalignment angle. The model is calibrated by adjusting the maximum initial misalignment angle so that the predicted strength matches the specimen strength The procedure for misaligment angle calibration is as follows: Multiple mesoscale simulations of the UD material were performed by varying the misalignment angle. A least-squares function was fitted to the resulting strength vs. misalignment angle data. The calibrated misalignment angle is read from the fitted curve as the value that corresponds to the mean UD compression strength measured in the experiments. The calibrated misalignment angle is 1.35°. The half-wavelength of the misalignment function is set to $l = 0.5$ mm (approximately 71 times the fiber diameter), which is shown to be a sufficient localization of fiber misalignment for kink band initiation based on the analyses of [33, 46, 79] and the experimental observations in [43, 72].

The stress-strain behavior obtained from 90 degree V-notch experiments were used to calibrate the failure properties of the matrix. The shear chord modulus (computed at 1 microstrain and 2 microstrain) and the ultimate specimen shear strength predicted by numerical simulations and mean experimental results were matched by calibrating $a^{(\mathrm{m})}$ and $b^{(\mathrm{m})}$. The calibration simulations consisted of a mesoscale finite element (a section of composite material) subjected to simple shear. The calibration is performed manually. The outcomes of the calibration simulations are listed in Table 3 alongside the experimental values. Given the variability observed in the experiments, reaching a minimum of 95% accuracy in capturing the mean is deemed sufficient to conclude the calibration process. With the calibrated matrix parameters, the resulting transverse composite compression strength is 91 MPa (found by subjecting a mesoscale finite element to uniaxial transverse displacement conditions at the nodes). The value for w used in Eq.10 is chosen such that the simulated kink band width is equal to the average kink band width measurements taken from micrograph images of a DENC specimen. The experimental target values and calibration simulation results are presented in Table 3. The influence of model parameters on the kink band width and strength predictions is studied in detail in Ref. [33].

The parameters of the cohesive zone model for splitting are also calibrated based on experimental observations and prior data. Table 4 shows the mode I and mode II maximum traction and fracture energies used in the simulations. The maximum traction values are estimated in the normal and shear directions based on values used in the literature for carbon-epoxy laminates [62, 75]. The initial stiffness, k_{coh}, is set to 10^5 N mm^{-3} (about 27 times the matrix elastic modulus) on the diagonal components and zero on the off-diagonal components. The stiffness value is on the order of

Table 2
Calibrated parameters of the kink band and local damage model (components designated in the local coordinate axes where the 1 direction designates the fiber direction).

Parameter	Unit	Value	Source	Parameter	Unit	Value	Source
$E_1^{(f)}$	GPa	305.0	UD DENC	$\nu_{12}^{(f)}$	N/A	0.206	[17]
$E_2^{(f)}$	GPa	12.45	[17]	$E^{(m)}$	GPa	3.70	[17]
$G_{21}^{(f)}$	GPa	146.0	[17]	$\nu^{(m)}$	N/A	0.377	[17]
$\nu_{23}^{(f)}$	N/A	0.291	[17]	ψ_0	°	1.35	UD DENC
$a^{(m)}$	$MPa^{-1/2}$	22.5	V-notch Shear	η	N/A	-2.0	[33]
$b^{(m)}$	N/A	17.5	V-notch Shear	c_1	N/A	0.833	UD/V-notch
$\kappa_0^{(m)}$	$\sqrt{MPa}$	0.0	[33]	c_2	N/A	-35.0	UD/V-notch
R	N/A	-0.006	[33]	w	μm	42.8	DENC

Table 3
Experimental and model composite properties.

Property	Experiment	Experimental Mean (standard deviation)	Calibration Simulation Result
Longitudinal Compression Strength (GPa)	UD DENC	1.43 (0.18)	1.43
Longitudinal Compression Modulus (GPa)	UD DENC	206.9 (5.39)	203.0
Ultimate Shear Strength (MPa)	V-notch shear	58.8 (19.1)	55.7
Shear Modulus (GPa)	V-notch shear	6.44 (0.39)	6.40

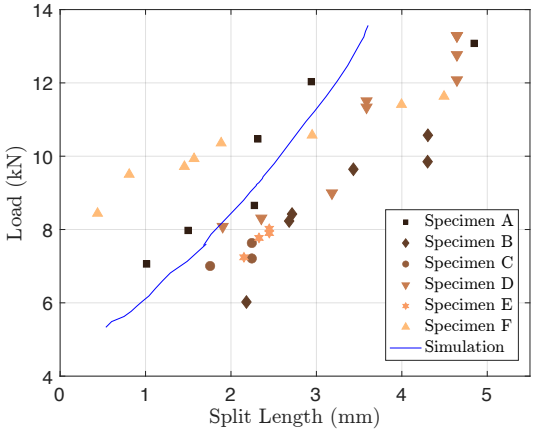

Figure 3: Experimental image analysis results overlaid with the calibration simulation result.

magnitude found to not significantly affect the compliance of the composite while also avoiding convergence issues in [76]. The critical fracture energies for splitting differ from those for delamination that are typically calibrated using double cantilever beam (DCB) and end notch flexure (ENF) tests. In particular, prior investigations determined that the critical mode II fracture energy for splits is approximately 25-40% [41, 52, 61] of measured G_{IIC}^{PC} from ENF tests (PC indicates the pre-cracked fracture toughness value). In accordance with these findings, we set G_{IIC}^{s} to be 1/4 the value of measured G_{IIC}^{PC} (=0.502 kJ/m^2). G_{IC}^{s} is set equal to G_{IC} from the DCB test results since other investigations indicate the split initiation and growth to be mode II driven fracture (see again [41, 52, 61]). The BK exponent, β, is set to 1.0 in the absence of critical fracture energy data for the IM7/977-3 material system under mixed-mode interlaminar or intralaminar conditions.

The model includes a pre-existing split ahead of the notch in the 0 degree plies as described above. A sensitivity study was performed to understand the effect of the length of the split introduced on the overall damage evolution behavior. In this study, the plies were assumed to remain elastic. This is consistent with experimental observations below, that indicate that splits are the first major damage event observed under compression. Fig. 3 shows the growth of the splits as a function of load amplitude based on the simulations and the experimental observations. The experimental observations are obtained from the analysis of optical images of the experimental DENC specimens. The initial split length and corresponding load level are tracked, providing a coarse representation of the split growth. Simulations were performed with pre-splits of lengths 0.125, 0.25, 0.50, 1.0, and 2.0 mm from the notch tip. The simulations recover the same curve regardless of the size of the initial split (the discontinuity at split length of 1.71 mm is due to combining results from simulations with short and long initial split lengths recorded from different mesh sizes) indicating that the growth behavior is not affected by the choice of the initial length.

An additional sensitivity analysis was performed to investigate the effect of fracture parameters for splitting on the rate of split growth. In this analysis, simulations were performed by setting G_{IIC}^{s} to values in the range of 0.10 to 0.20 kJ/m^2 and ultimate traction to values in the range of 90 to 180 MPa. The rate of split growth is found not to be affected significantly by G_{IIC}^{s} or the ultimate traction values. These parameters were found to have a stronger influence on the load at which splits initiate. This observation is consistent with those reported in [61]. Since the experimental data exhibits large variation, the splitting model is calibrated such that the crack growth curve fits through the mean experimental initial split length and load values. The slope

Table 4
Parameters of the cohesive zone model.

Parameter	Unit	Value	Source	Parameter	Unit	Value	Source
k_{coh}	N/mm^3	10^5	[47, 76]	G^s_{IC}	kJ/m^2	0.230	DCB
t^0_I	MPa	60	[62]	G^s_{IIC}	kJ/m^2	0.130	ENF
t^0_{II}	MPa	90	[75]	β	N/A	1.0	Estimate

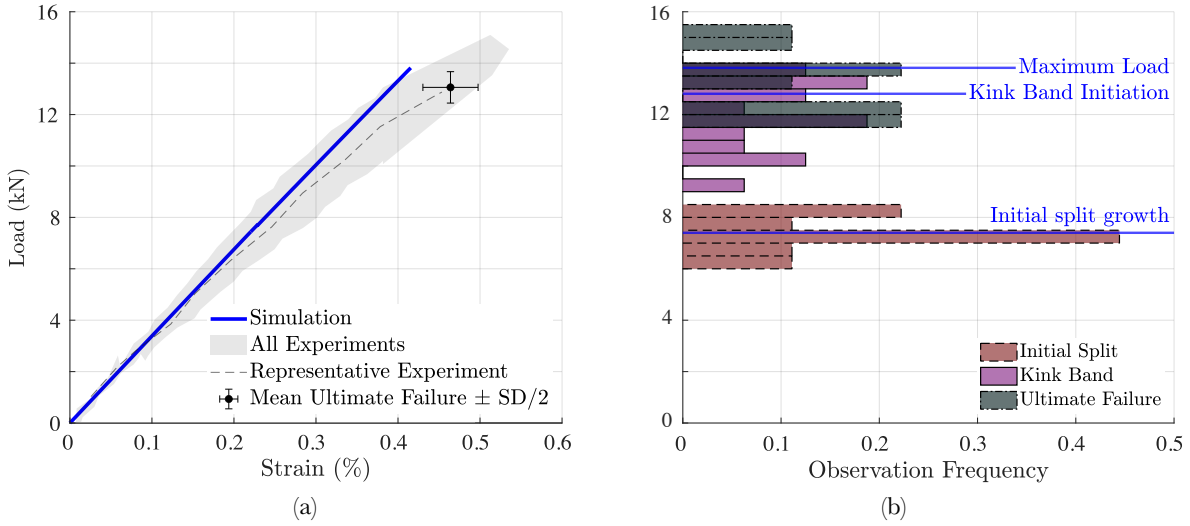

Figure 4: (a) Load-strain predictions compared to experimental results; (b) mechanism and failure observation loads (bars) and predictions (annotated solid lines).

of the load vs. split length predicted by the model falls within the observed experimental data as shown in Fig. 3.

3.2. Analysis of DENC Behavior

Simulation of the DENC specimen was performed using the calibrated model parameters and completed in about 81 hours using 8 processors in parallel. Results from the simulation were analyzed along with the experimental observations. Figure 4a shows the envelope of load vs. strain curves from specimens ran to failure in addition to the interrupted tests and the calibrated simulation prediction. Simulated strains are computed by mimicking the virtual extensometer measurements. The base length of the virtual extensometer is 3.0 mm and the macroscopic strain is calculated as the difference between the average displacements of nodes within a 40 µm radius of the two extensometer ends. In Fig. 4b, the histograms for the observation of initial splits, kink bands, and failure in terms of load amplitude in the DENC experiments and simulation are shown. The predicted macroscopic force response is essentially linear until an unstable load drop suggesting an abrupt failure process. The maximum load prediction (13.8 kN) is within the range observed in the experiments (11.7-15.1 kN) and somewhat overpredicts the mean (13.1 kN). The experiment results exhibit a somewhat nonlinear macroscopic load-strain response and the strain at maximum load ranges from 0.37% to 0.54% (mean 0.46%) while the predicted strain at maximum load is 0.42%. The standard deviation of the failure loads and strains is also plotted on Fig. 4a.

Nonlinearity in the DENC experiments initiates early on and continues throughout the loading process until failure, as demonstrated by the representative experiment curve in Fig. 4. This nonlinearity is likely due to nonlinear shear effects, although additional mechanisms could be contributing to this behavior as discussed below. Other experimental studies in the literature report similar nonlinearity in the compressive stress-strain response of laminates [13, 45, 66] (e.g., in laminates with high volume fraction of 45 degree plies and when 0 degree plies are not at the mid-plane [45, 66]). The amount of nonlinearity varies with specimen size, presence of off axis plies, ply thickness, and layup.

In the DENC model, the matrix constitutive behavior was calibrated (as described in Section 3.1) based on 90 degree V-notch shear tests which exhibit a relatively brittle behavior (specimen failure around 1-2% shear strain). Other experiments including ± 45 degree tension and V-notch shear [17, 40] show higher ductility, which could better characterize the nonlinear shear behavior of the composite. For instance, Ref. [17] demonstrated an alternative matrix damage model which directly incorporates shear nonlinearity and uses both sets of shear tests to calibrate the matrix model.

Nonlinearity in the fiber behavior was also previously proposed to contribute to the observed nonlinearity of the overall compressive stress-strain curve [48, 64]. The model in Ref. [13] includes nonlinearity in the longitudinal lamina modulus using the empirical relationship from Ref. [42], however the importance of it in determining the nonlinear

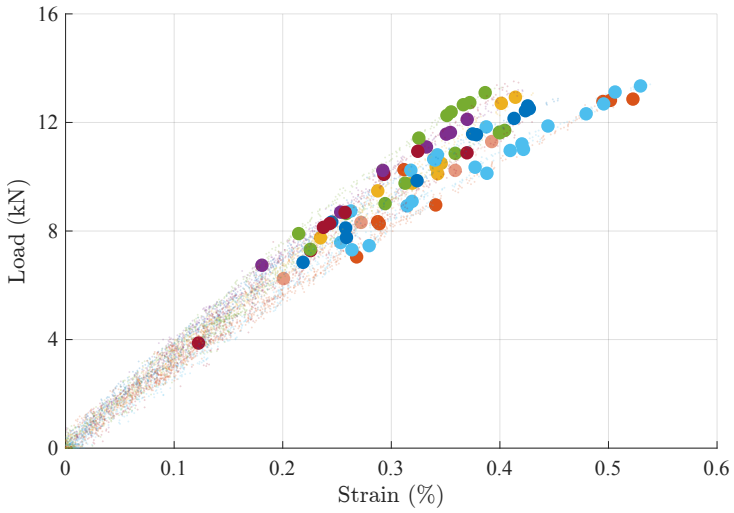

Figure 5: Acoustic energy-events during loading in all experiments. The large markers indicate acoustic events meeting or exceeding the observable damage threshold and the small markers indicate acoustic events below the threshold (each color represents a different test).

macroscopic response is not studied. Other studies on multidirectional laminates under compression incorporate fiber damage [12, 17] but predict fiber failure only above 90% of the ultimate load.

Acoustic emission sensors were used to provide additional information on the evolution of damage in the specimens. Acoustic energy-event histories from all of the experiments are shown in Fig. 5 where the events which meet or exceed the observable damage threshold are plotted with large opaque markers while smaller acoustic energy events are plotted with small faint markers. Smaller acoustic energy events are numerous and present throughout the entire loading process. The earliest damage event observed in the experiments is split formation at the range of 6-8.5 kN. There are relatively few and spread out observable damage events after the onset of nonlinearity. Images from specimens with these readings included evidence of one or more compression failure mechanisms.

Evidence of the failure mechanisms in the 45 degree plies of the test specimens is compared to model predictions in Fig. 6. Figure 6a shows damage regions in a failed specimen loaded to 13.2 kN. There is a longitudinally-extending damage feature at the left notch while a 45 degree feature present at the right notch. Higher magnification images of the left notch in Fig. 6b show details of the damage features observed from the same specimen scanned with dye penetrant introduced. The images include thin matrix cracking patterns in addition to a stepped failure propagation. The stepped feature shown in Fig. 6a is also present in Fig. 6b Detail 1 (labeled “I") and likely consists of matrix cracks which migrate around fibers but might also include broken fibers. The saturated area in Detail 1 (labeled “II" in Fig. 6b) could be delamination or a dense field of matrix cracks parallel to the 45 degree fibers. In addition to the distinct crack originating at the bottom of the notch in Detail 2 (labeled “III"), there are multiple cracks parallel to the fiber direction above the notch location (labeled “IV"). The highlights oriented perpendicular to the fiber direction in this region are the results of cracks in the adjacent 45 degree ply. The X-ray CT images also include beam-hardening artifacts as indicated in the Fig. 6a-b. The artifacts in Fig. 6a are caused by the notch edge, which is parallel to the X-ray beam path and spans from the left to the right side of the image. The artifacts in Fig. 6b appearing as thick and dark vertical strips are caused by the presence of dye penetrant and large variations of the X-ray attenuation within the material of the scanned volume around the notch tip. In comparison, the model predicts matrix damage in the 45 degree plies as shown in Fig. 6c. Full matrix damage is present prior to 10.2 kN, and grows from the split. Distinct damage paths are predicted at the ultimate load of 13.8 kN, propagating in the space between the notches. The model also predicts damage along and behind the splits. Overall, the damage contours are similar to the experiment images with dye-penetrant which show a combination of distinctly isolated cracks in addition to different forms of less isolated damage features and paths.

Splitting is observed in the experiments as shown on a representative specimen in Fig. 7a and Fig. 7c. In the experiments, initial splits (as observed after the first significant AE reading) are 1-2 mm long. Additional splits also develop at higher loads. In the specimen shown in Fig. 7a, splitting occurs first on the right notch, followed by the formation of a second and longer split on the left notch. The two splits grow toward the gripped boundaries with increasing loading in a stepwise and non-uniform manner as shown in the datasets in Fig. 3. It is not clear if the splits extend under the grips which were not imaged. The simulation predicts a nearly symmetric (due to the symmetry of the numerical specimen) growth of splits at the notches starting at 7.4 kN. The arrows in Fig. 7b indicate the split ends and the length evolution is similar to Fig. 3. At the load amplitude of 13.3 kN the dominant splits in both the

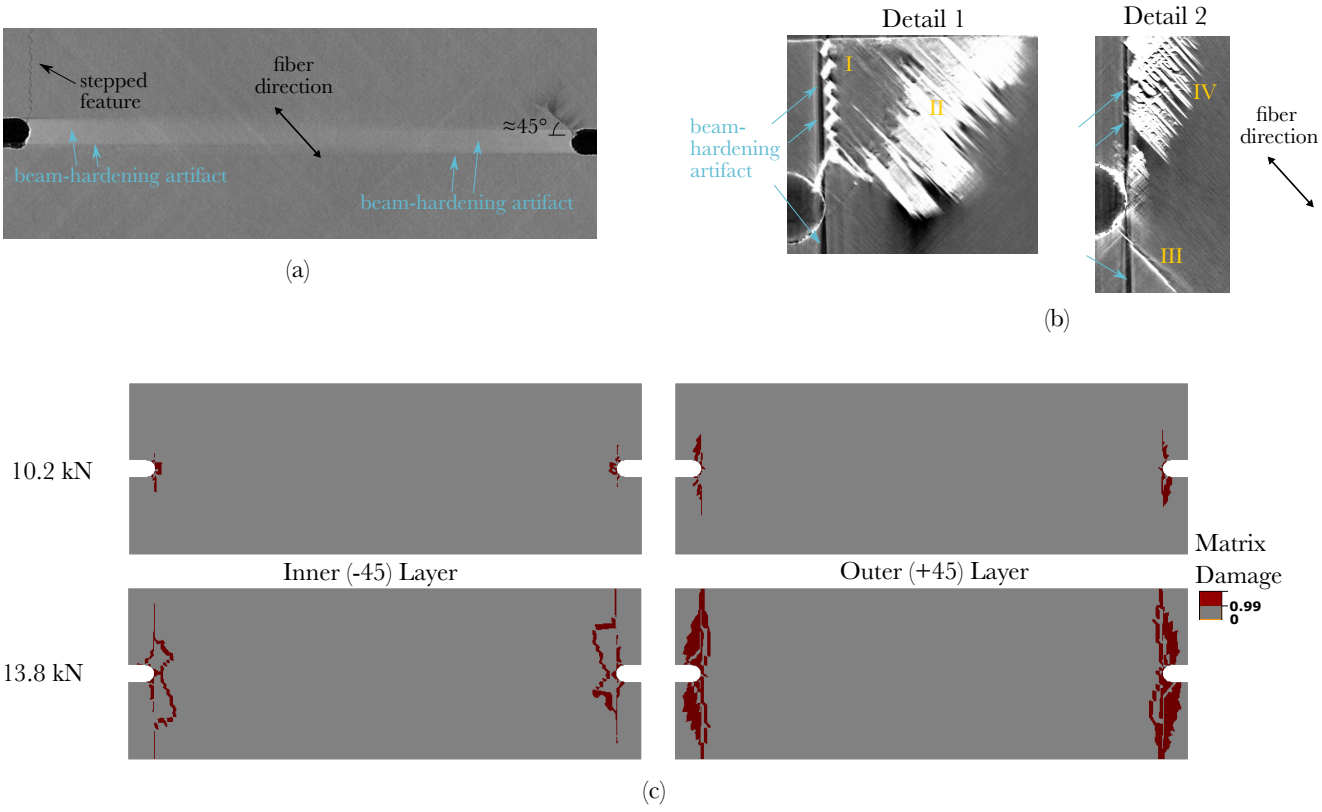

Figure 6: (a) Damage in 45 degree plies in an X-ray CT image. (b) Detailed images from scanning with dye penetrant. (c) Predicted damage patterns in the simulation.

experiment and the simulation are near or at the gripped boundaries. The lack of symmetry of the split formation and growth in the experiments is attributed to nonuniformity in the material. The shear concentration site on the notch with the weakest material will be where the first split forms. Additional split nucleation and split growth is dictated by the stress redistribution thereafter. The highlighting from the dye penetrant in X-ray CT images in Fig. 8a-b demonstrates the most frequently observed splitting pattern in the 0 degree plies at loads over 13 kN. Splits are consistently present in the exterior plies and observed with much less frequency in the interior 0 degree plies. The simulation also predicts prominent splitting in the exterior plies, and the predicted split growth is smaller in the interior 0 degree layer as shown in Fig. 8c.

Figure 9 shows the longitudinal strain fields in the exterior and interior 0 degree plies during the simulation near the predicted failure load. The simulation predicts the onset of the kink band at the interior 0 degree ply around 12.8 kN (92.7% of the ultimate load). There is a progressive and steady propagation of the kink band from the onset until the ultimate load is reached. Concentration of higher magnitude longitudinal strains ahead of the notch tip is evident in the interior ply plots. The strains immediately above and below the formed kink band are relaxed behind the kink band front. The propagation then accelerates and instantaneously leads to specimen failure. In the experiments, the nucleation time of the kink bands cannot be determined with accuracy since kink band observations were made in interrupted tests, which were not taken to failure, since these specimens were sacrificed to sectioning for kink band characterization. Kink bands are observed in the experiments starting in specimens reaching loads of 10.6 kN and higher. The predicted macroscopic strain at kink band initiation of 0.38% lies towards the upper bound of strains experienced in the experiments at loads around 10.6 kN (0.29-0.40%). The large range of strains associated with observed kink band formation implies that there is variability in the failure onset time. The majority of specimens did not show formation or propagation of kink bands in the exterior 0 degree plies and an example of the through-thickness kink band presence is shown in Fig. 8a-b. The longitudinal strain in the middle 0 degree plies of the specimen is shown in Fig. 10a with close up profiles of matrix damage in the cross-section ahead of the notch (Section A-A) and at the kink band tip (Section B-B). The damage patterns reflect what is observed in the experiments, where micrograph sections show clear matrix cracking in the plus/minus 45 degree and 90 degree plies near the root of the kink band ahead of the notch as shown in the micrograph section Fig. 10b and only the kink band further away from the notch like shown in Fig. 10c. The experiment images in Fig. 10b-c clearly show that the primary kink band propagation occurs in the interior 0 degree ply only and additional numerical simulations we performed suggests that splitting affects the observed behavior. For instance, in the absence of splits the

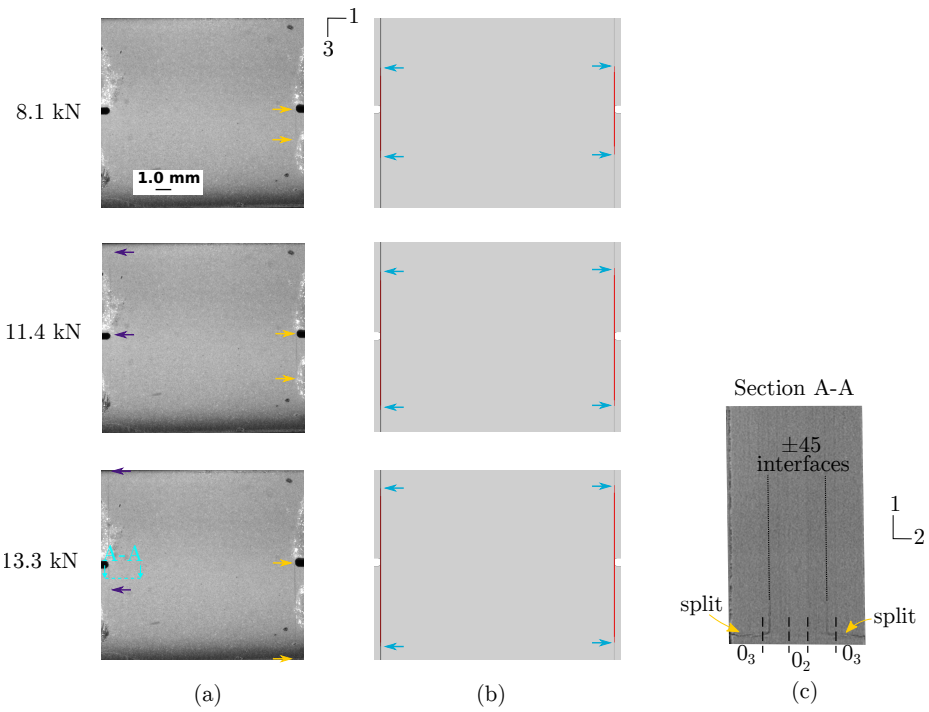

Figure 7: Split evolution in the exterior plies in the (a) experiments and (b) simulation (arrows indicate ends of the splits). (c) Through-thickness splitting in an X-ray CT image from the experiment.

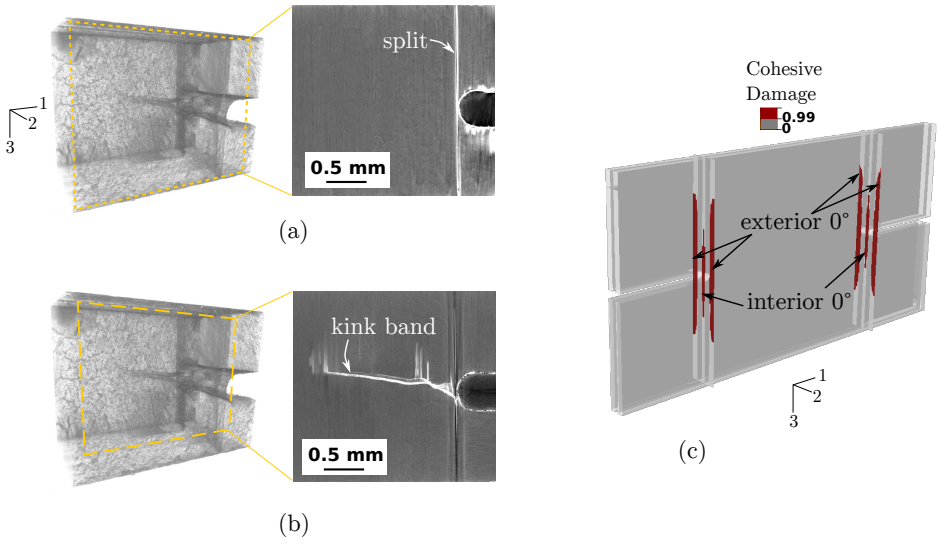

Figure 8: X-ray CT images of a dye penetrated specimen loaded to 13.2 kN showing (a) splitting in the exterior 0 degree ply and (b) kink band interior 0 degree ply. (c) Through-thickness splitting predicted at ultimate load.

kink bands initiate in the exterior plies first, around 7.9 kN, and propagate ahead of later-initiating kink bands in the interior plies until failure. Suppressing splitting results in a significant under-prediction of the failure load (8.3 kN) and the strain at failure (0.33%) pointing to the relaxation induced by the splits. Splits forming 20-50 μm behind the notch tip increases the load and strain at failure but still under-predicts the experimental range.

X-ray CT images additionally suggest delamination between the 0 and 90 degree plies connected to the ends of the kink band as shown in Fig. 11a. The delaminations present at the 0-90 degree ply interface extend parallel to the kink band propagation and likely formed to accommodate the discontinuity induced by the kink band ends. These delaminations were not modeled explicitly in the simulations. Incorporating this mechanism with cohesive elements results in convergence issues and excessive computation times making the analysis infeasible. Zooming into the model prediction at the kink band tip, Fig. 11b-c show the shear strains in the

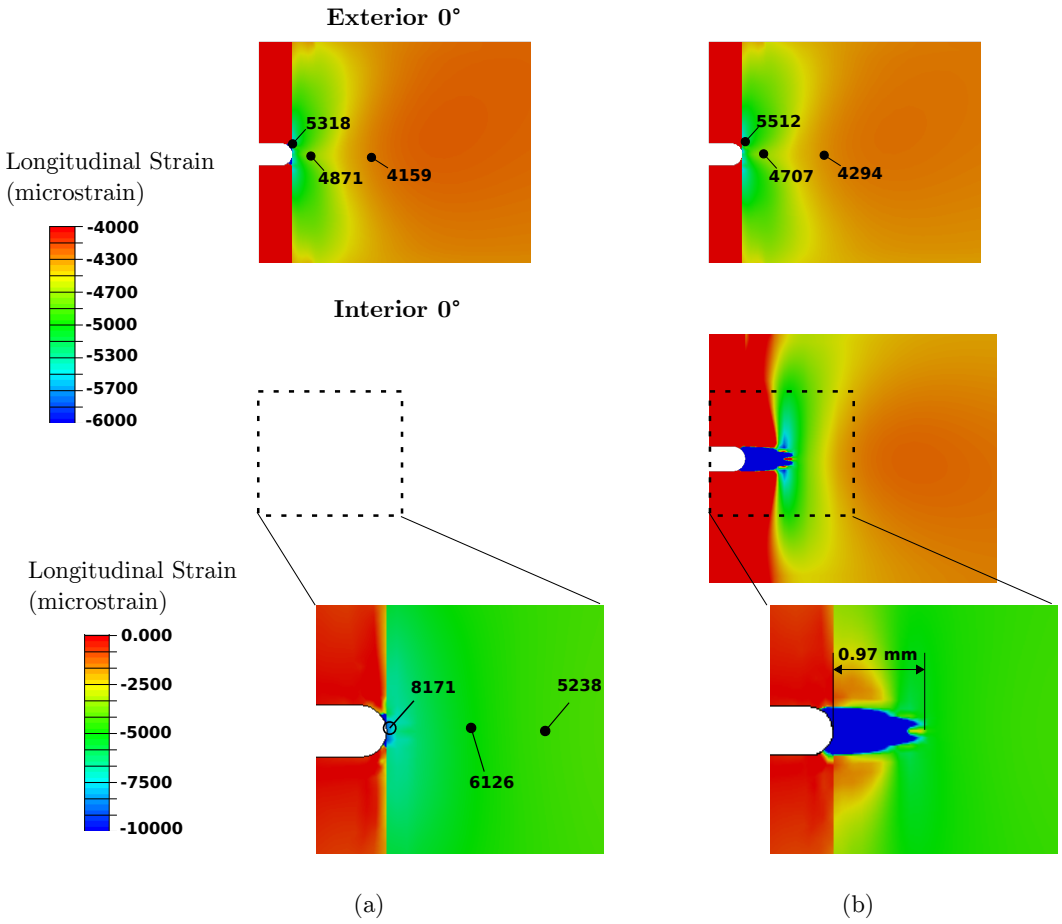

Figure 9: Predicted longitudinal strain fields in the 0 degree plies at (a) 92.7% of the ultimate load and (b) ultimate load. Strains are reported in the global coordinate system.

through-thickness cross section. There is significant shearing (ε_{12} and ε_{23}) present at the 0-90 degree ply interfaces at the ends of the kink band. This information suggests that the onset of delaminations is likely shear driven. The 45 degree plies experience shearing (ε_{23}) as well, coinciding with the predicted matrix damage pattern in Fig. 10a, Section A-A, suggesting that the damage at the ±45 degree interface visible in Fig. 11a and Fig. 7c is shear driven.

4. Conclusions

Analysis of images from DENC experiments provide some indication of the load levels where splitting and kink bands are present. Simulation results point to the capabilities of the multiscale modeling approach and enhance the understanding of these failure mechanisms in the DENC ultimate failure while greatly reducing computational cost compared to a direct numerical simulation of fibers and matrix. The lamina behavior in the model was calibrated using UD-DENC compression and V-notch shear properties. Measurements from micrograph and optical images were used to select parameter values related to kink band width and splitting behavior. The model predicts the DENC failure load within the range of experimental values and shows how the critical failure mechanism of kink bands occurring primarily on the interior of the specimen, and interior and exterior occurring subcritical damage features interact during the failure process. Among the consistently observed failure mechanisms, splitting is particularly important as the formation of splits directly alters the stress distribution around the notches. Matrix cracking in the 45 degree plies is predicted to accompany splitting just ahead of the notches in agreement with experimental cross-sectional images obtained from specimens loaded to ultimate failure. The onset of matrix damage is not clear from the experimental images but the model predicts early onset around the onset time of splits. Together, these precursors to ultimate failure contribute to the load range where instability of the inner 0 degree layer results in kink band initiation around 93% of the ultimate predicted macroscopic load and propagation between both notches. Splits not present or forming behind the notch tip result in an under-prediction of the experimentally observed kink band and ultimate loads.

The numerical predictions suggest that the simultaneous presence of matrix cracking, exterior ply splits and kink bands should be considered in modeling laminates with exterior 0 degree plies in order to accurately capture the apparent strength, failure propagation, and failure interactions. Additionally, while delamination is not included in the

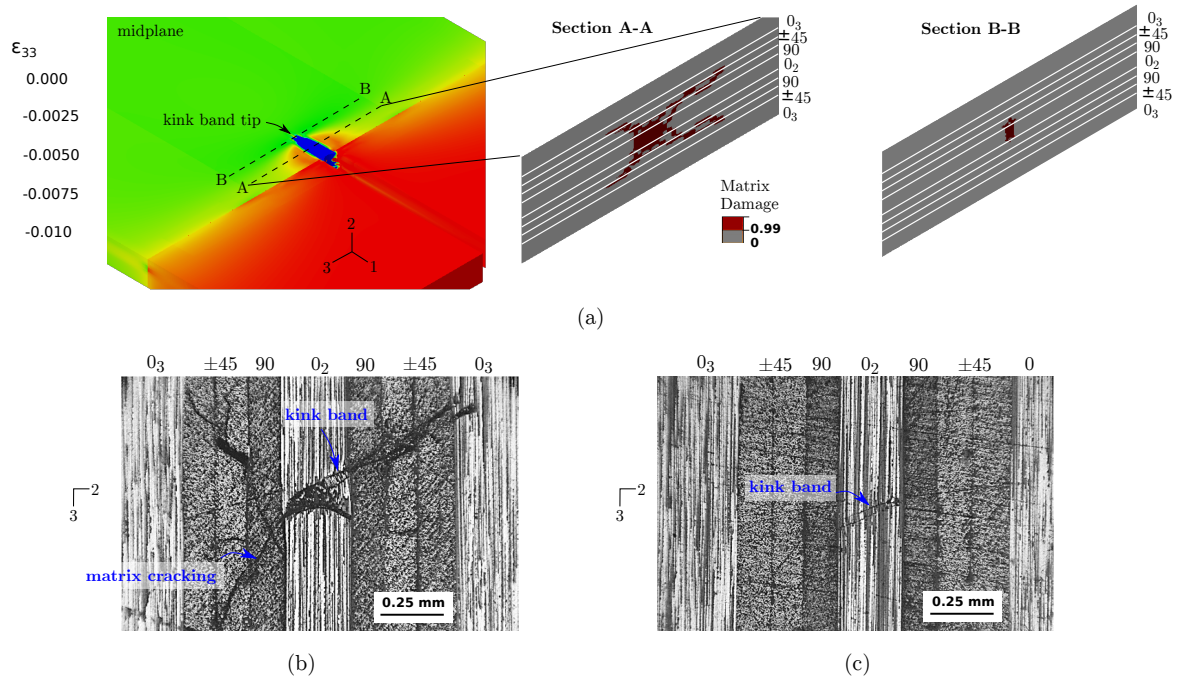

Figure 10: (a) Damage prediction in a cross-section parallel to the 2-3 plane. Micrographs of the same perspective in a specimen loaded to 12.9 kN located (b) just ahead of the notch and (c) at the kink band tip (approx. 2.1 mm ahead of the notch tip).

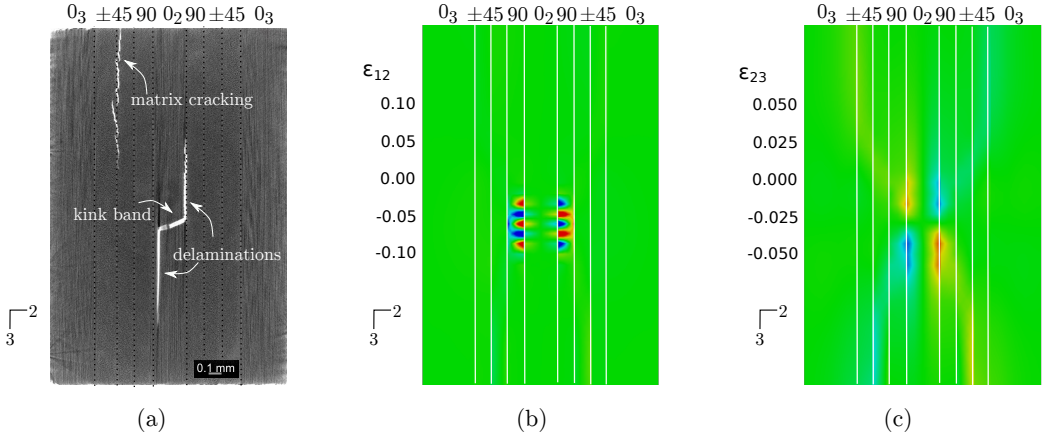

Figure 11: (a) X-ray CT image of the same perspective in Fig. 10 and within the kink band, about 1.5 mm ahead of the notch tip. Predicted shear strain (b) 1-2 and (c) 2-3. Strains are reported in the global coordinate system.

final simulations due to excessive computational demand, significant shear straining is predicted at the 90-0 degree ply interfaces and 45 degree plies prior to ultimate load. Without predicting the progression of delamination, the model predicts kink band propagation as the cause of ultimate failure, matching experimental observations which also indicate the subcritical nature of delaminations (occurring at the interfaces bounding the primary kink band [23, 66]).

The proposed multiscale computational model does not capture the nonlinearity observed in the overall load-strain behavior of the composite. The potential sources of this nonlinearity are discussed in the manuscript. A thorough and quantitive investigation of all sources of nonlinearity is necessary. Such an investigation could be used to extend the multiscale model and address this shortcoming.

Because of the multitude of failure modes and size of the model, we were not able to perform parametric analyses (e.g. with fiber waviness characteristics or matrix shear nonlinearity) or predict the progression of delamination with the DENC model.

The experimental data show a strong variation of matrix cracking pattern ahead of the notch tip in addition to splitting and kink band onset time. A probabilistic sampling of material properties that reflect material heterogeneity and uncertainty in model parameters could provide insight to the sources of variation of experiment load-strain results. Future work could include parametric studies to investigate different sources for the macroscopic nonlinearity in the overall load-strain results, and incorporate delamination progression well.

5. Funding and Acknowledgements

The authors gratefully acknowledge the financial support of the Air Force Research Laboratory SIRCA Award No: FA8650-19-2-2214. The authors also acknowledge support of the USA-Israel Air Vehicle Technologies Project Agreement (AVT PA). Specifically, the authors would like to thank Ido Meshi (PhD Student at Tel-Aviv University) for discussions during the finite element model design and Ofir Shor of Rafael Advanced Defense Systems Ltd. who spent many days performing the microCT scans, obtaining the best parameters for each scan and each magnification, and performing image extraction and data analysis.

CRediT authorship contribution statement

Alex Faupel: Conceptualization; Data curation; Formal analysis; Investigation; Methodology; Software; Validation; Visualization; Roles/Writing - original draft. **Caglar Oskay:** Conceptualization; Funding acquisition; Methodology; Project administration; Formal analysis; Writing - review and editing.

References

[1] Andrade, F., de Sá, J.C., Pires, F.A., 2014. Assessment and comparison of non-local integral models for ductile damage. International Journal of Damage Mechanics 23, 261–296. URL: https://doi.org/10.1177/1056789513493103, doi:10.1177/1056789513493103, arXiv:https://doi.org/10.1177/1056789513493103.

[2] Argon, A.S., 1972. Fracture of Composites. Treatise on Materials Science and Technology 1, 79–114.

[3] ASTM D5379/D5379M-19e1, 2021. Shear Properties of Composite Materials by the V-Notched Beam Method. Standard. ASTM International. doi:10.1520/D5379_D5379M-19E01.

[4] ASTM D5528/D5528M-21, 2022. Determination of the Mode I Interlaminar Fracture Toughness of Unidirectional Fiber-Reinforced Polymer Matrix Composites. Standard. ASTM International. doi:10.1520/D5528_D5528M-21.

[5] ASTM D6641/D6641M-16e2, 2021. Compressive Properties of Polymer Matrix Composite Materials Using a Combined Loading Compression (CLC) Test Fixture. Standard. ASTM International. doi:10.1520/D6641_D6641M-16E02.

[6] ASTM D7905/D7905M-19e1, 2019. Determination of the Mode II Interlaminar Fracture Toughness of Unidirectional Fiber-Reinforced Polymer Matrix Composites. Standard. ASTM International. doi:10.1520/D7905_D7905M-19E01.

[7] Basu, S., Waas, A.M., Ambur, D.R., 2006. Compressive failure of fiber composites under multi-axial loading. Journal of the Mechanics and Physics of Solids 54, 611 – 634. URL: http://www.sciencedirect.com/science/article/pii/S0022509605001948, doi:https://doi.org/10.1016/j.jmps.2005.09.004.

[8] Benzeggagh, M., Kenane, M., 1996. Measurement of mixed-mode delamination fracture toughness of unidirectional glass/epoxy composites with mixed-mode bending apparatus. Composites science and technology 56, 439–449.

[9] Bergan, A.C., Garcea, S.C., 2017. In-Situ Observations of Longitudinal Compression Damage in Carbon-Epoxy Cross Ply Laminates Using Fast Synchrotron Radiation Computed Tomography. Technical Report. NASA. URL: https://ntrs.nasa.gov/citations/20170010325.

[10] Bergan, A.C., Herráez, M., González, C., Lopes, C.S., 2020a. A constitutive model for fiber kinking: Formulation, finite element implementation, and verification. Composites Part A: Applied Science and Manufacturing 129, 105682. URL: https://www.sciencedirect.com/science/article/pii/S1359835X19304312, doi:https://doi.org/10.1016/j.compositesa.2019.105682.

[11] Bergan, A.C., Leone, F.A., 2016. A Continuum Damage Mechanics Model to Predict Kink-Band Propagation Using Deformation Gradient Tensor Decomposition. Technical Report. NASA. URL: https://ntrs.nasa.gov/citations/20160012045.

[12] Bergan, A.C., Murphy, S.J., Miles, L.F., 2020b. Analysis of Open Hole Compression Specimens Using the CompDam Continuum Damage Mechanics Model. Technical Memorandum. NASA. URL: https://ntrs.nasa.gov/citations/20205009618.

[13] Bergan, A.C., Wade, J.C., 2019. Validation of a Mesoscale Fiber Kinking Model through Test and Analysis of Double Edge Notch Compression Specimens. Technical Report. NASA. URL: https://ntrs.nasa.gov/archive/nasa/casi.ntrs.nasa.gov/20190033161.pdf.

[14] Bishara, M., Rolfes, R., Allix, O., 2017. Revealing complex aspects of compressive failure of polymer composites – part i: Fiber kinking at microscale. Composite Structures 169, 105 – 115. URL: http://www.sciencedirect.com/science/article/pii/S026382231632222X, doi:https://doi.org/10.1016/j.compstruct.2016.10.092. in Honor of Prof. Leissa.

[15] Bishara, M., Vogler, M., Rolfes, R., 2016. Revealing complex aspects of compressive failure of polymer composites - part ii: Failure interactions in multidirectional laminates and validation. Composite Structures 169. doi:10.1016/j.compstruct.2016.10.091.

[16] Bogdanor, M.J., Clay, S.B., Oskay, C., 2019. Interacting damage mechanisms in laminated composites subjected to high amplitude fatigue. Journal of Engineering Mechanics .

[17] Bogdanor, M.J., Oskay, C., 2017a. Prediction of progressive damage and strength of IM7/977-3 composites using the eigendeformation-based homogenization approach: Static loading. Journal of Composite Materials 51, 1455–1472. URL: https://doi.org/10.1177/0021998316650982, doi:10.1177/0021998316650982, arXiv:https://doi.org/10.1177/0021998316650982.

[18] Bogdanor, M.J., Oskay, C., 2017b. Prediction of progressive fatigue damage and failure behavior of IM7/977-3 composites using the reduced-order multiple space-time homogenization approach. J. Composite Mater. 51, 2101–2117.

[19] Budiansky, B., Fleck, N., 1993. Compressive failure of fibre composites. Journal of the Mechanics and Physics of Solids 41, 183,211.

[20] Camanho, P., Arteiro, A., Melro, A., Catalanotti, G., Vogler, M., 2015. Three-dimensional invariant-based failure criteria for fibre-reinforced composites. International Journal of Solids and Structures 55, 92–107. URL: https://www.sciencedirect.com/science/article/pii/S0020768314001449, doi:https://doi.org/10.1016/j.ijsolstr.2014.03.038. special Issue Computational and Experimental Mechanics of Advanced Materials A workshop held at King Abdullah University of Science and Technology Jeddah, Kingdom of Saudi Arabia July 1-3, 2013.

[21] Camanho, P., Bessa, M., Catalanotti, G., Vogler, M., Rolfes, R., 2013. Modeling the inelastic deformation and fracture of polymer composites – part ii: Smeared crack model. Mechanics of materials 59, 36–49.

[22] Camanho, P., Dávila, C., 2002. Mixed-Mode Decohesion Finite Elements for the Simulation of Delamination in Composite Materials. Technical Report. NASA. URL: https://ntrs.nasa.gov/citations/20020053651.

[23] Clay, S., Ault, W., Faupel, A., Oskay, C., Knoth, P., Shemesh, N.N., Haj-Ali, R., Breiman, U., Meshi, I., Shor, O., 2024. Experimental characterization of compression failure mechanism initiation and growth in notched carbon fiber reinforced composite specimens. Composites Part A: Applied Science and Manufacturing 176, 107865. URL: https://www.sciencedirect.com/science/article/pii/S1359835X23004414, doi:https://doi.org/10.1016/j.compositesa.2023.107865.

[24] Clay, S.B., Knoth, P.M., 2017. Experimental results of quasi-static testing for calibration and validation of composite progressive damage analysis methods. Journal of Composite Materials 51, 1333–1353. URL: https://doi.org/10.1177/0021998316658539, doi:10.1177/

0021998316658539, arXiv:https://doi.org/10.1177/0021998316658539.

[25] Crouch, R.D., Clay, S.B., Oskay, C., 2013a. Experimental and computational investigation of progressive damage accumulation in cfrp composites. Compos. Part B: Eng. 48, 59–67.

[26] Crouch, R.D., Oskay, C., Clay, S.B., 2013b. Multiple spatio-temporal scale modeling of composites subjected to cyclic loading. Comp. Mech. 51, 93–107.

[27] Cui, X., Fang, E., Lua, J., 2017. A discrete crack network toolkit for abaqus for damage and residual strength prediction of laminated composites. Journal of Composite Materials 51, 1355–1378. URL: https://doi.org/10.1177/0021998316659914, doi:10.1177/0021998316659914, arXiv:https://doi.org/10.1177/0021998316659914.

[28] de Borst, R., 2003. Numerical aspects of cohesive-zone models. Engineering Fracture Mechanics 70, 1743–1757. URL: https://www.sciencedirect.com/science/article/pii/S001379440300122X, doi:https://doi.org/10.1016/S0013-7944(03)00122-X.

[29] Falcó, O., Ávila, R., Tijs, B., Lopes, C., 2018. Modelling and simulation methodology for unidirectional composite laminates in a virtual test lab framework. Composite Structures 190, 137–159. URL: https://www.sciencedirect.com/science/article/pii/S0263822317329768, doi:https://doi.org/10.1016/j.compstruct.2018.02.016.

[30] Falkowicz, K., 2023a. Experimental and numerical failure analysis of thin-walled composite plates using progressive failure analysis. Composite Structures 305, 116474. URL: https://www.sciencedirect.com/science/article/pii/S0263822322012065, doi:https://doi.org/10.1016/j.compstruct.2022.116474.

[31] Falkowicz, K., 2023b. Validation of extension-bending and extension-twisting coupled laminates in elastic element. Advances in Science and Technology Research Journal 17, 309–319. URL: https://doi.org/10.12913/22998624/167451, doi:10.12913/22998624/167451.

[32] Falkowicz, K., Debski, H., 2019. The work of a compressed, composite plate in asymmetrical arrangement of layers. AIP Conference Proceedings 2078, 020005. URL: https://doi.org/10.1063/1.5092008, doi:10.1063/1.5092008.

[33] Faupel, A., Meshi, I., Oskay, C., 2022. Reduced order multiscale model for compression kink-band failure in composites. Journal of Composite Materials 56, 3385–3400. URL: https://doi.org/10.1177/00219983221114012, doi:10.1177/00219983221114012, arXiv:https://doi.org/10.1177/00219983221114012.

[34] Fleck, N.A., Deng, L., Budiansky, B., 1995. Prediction of Kink Width in Compressed Fiber Composites. Journal of Applied Mechanics 62, 329–337. URL: https://doi.org/10.1115/1.2895935, doi:10.1115/1.2895935.

[35] Geers, M., de Borst, R., Brekelmans, W., Peerlings, R., 1998. Strain-based transient-gradient damage model for failure analyses. Computer Methods in Applied Mechanics and Engineering 160, 133–153. URL: https://www.sciencedirect.com/science/article/pii/S004578259880011X, doi:https://doi.org/10.1016/S0045-7825(98)80011-X.

[36] Gutkin, R., Pinho, S., Robinson, P., Curtis, P., 2010. On the transition from shear-driven fibre compressive failure to fibre kinking in notched cfrp laminates under longitudinal compression. Composites Science and Technology 70, 1223–1231. URL: https://www.sciencedirect.com/science/article/pii/S0266353810001119, doi:https://doi.org/10.1016/j.compscitech.2010.03.010.

[37] Hallett, S., Green, B., Jiang, W., Wisnom, M., 2009. An experimental and numerical investigation into the damage mechanisms in notched composites. Composites Part A: Applied Science and Manufacturing 40, 613–624. URL: https://www.sciencedirect.com/science/article/pii/S1359835X09000499, doi:https://doi.org/10.1016/j.compositesa.2009.02.021.

[38] Hoos, K., Iarve, E.V., Braginsky, M., Zhou, E., Mollenhauer, D.H., 2017. Static strength prediction in laminated composites by using discrete damage modeling. Journal of composite materials 51, 1473–1492.

[39] Hui, T., Oskay, C., 2012. Computational modeling of polyurea-coated composites subjected to blast loads. J. Compos. Mater. 46, 2167–2178.

[40] Kaddour, A., Hinton, M., 2012. Input data for test cases used in benchmarking triaxial failure theories of composites. Journal of Composite Materials 46, 2295–2312. URL: https://doi.org/10.1177/0021998312449886, doi:10.1177/0021998312449886, arXiv:https://doi.org/10.1177/0021998312449886.

[41] Kortschot, M., Beaumont, P., Ashby, M., 1991. Damage mechanics of composite materials. iii: Prediction of damage growth and notched strength. Composites Science and Technology 40, 147–165. URL: https://www.sciencedirect.com/science/article/pii/0266353891900946, doi:https://doi.org/10.1016/0266-3538(91)90094-6.

[42] Kowalski, I., 1988. Characterizing the tensile stress-strain nonlinearity of polyacrylonitrile-based carbon fibers, in: Composite Materials: Testing and Design (Eighth Conference). ASTM International, 100 Barr Harbor Drive, PO Box C700, West Conshohocken, PA 19428-2959, pp. 205–216.

[43] Kyriakides, S., Arseculeratne, R., Perry, E., Liechti, K., 1995. On the compressive failure of fiber reinforced composites. International Journal of Solids and Structures 32, 689 – 738. URL: http://www.sciencedirect.com/science/article/pii/002076839400157R, doi:https://doi.org/10.1016/0020-7683(94)00157-R. time Dependent Problems in Mechanics.

[44] Le, M., Bainier, H., Néron, D., Ha-Minh, C., Ladevèze, P., 2018. On matrix cracking and splits modeling in laminated composites. Composites Part A: Applied Science and Manufacturing 115, 294–301. URL: https://www.sciencedirect.com/science/article/pii/S1359835X18303920, doi:https://doi.org/10.1016/j.compositesa.2018.10.002.

[45] Lee, J., Soutis, C., 2007. A study on the compressive strength of thick carbon fibre–epoxy laminates. Composites Science and Technology 67, 2015–2026. URL: https://www.sciencedirect.com/science/article/pii/S0266353806004520, doi:https://doi.org/10.1016/j.compscitech.2006.12.001.

[46] Liu, D., Fleck, N., Sutcliffe, M., 2004. Compressive strength of fibre composites with random fibre waviness. Journal of the Mechanics and Physics of Solids 52, 1481 – 1505. URL: http://www.sciencedirect.com/science/article/pii/S0022509604000110, doi:https://doi.org/10.1016/j.jmps.2004.01.005.

[47] Lu, X., Ridha, M., Tan, V., Tay, T., 2019. Adaptive discrete-smeared crack (a-disc) model for multi-scale progressive damage in composites. Composites Part A: Applied Science and Manufacturing 125, 105513. URL: https://www.sciencedirect.com/science/article/pii/S1359835X19302623, doi:https://doi.org/10.1016/j.compositesa.2019.105513.

[48] Macturk, K., Eby, R., Adams, W., 1991. Characterization of compressive properties of high-performance polymer fibres with a new microcompression apparatus. Polymer (Guildford) 32, 1782–1787.

[49] Moran, P., Liu, X., Shih, C., 1995. Kink band formation and band broadening in fiber composites under compressive loading. Acta Metallurgica et Materialia 43, 2943 – 2958. URL: http://www.sciencedirect.com/science/article/pii/095671519500001C, doi:https://doi.org/10.1016/0956-7151(95)00001-C.

[50] Moran, P., Shih, C., 1998. Kink band propagation and broadening in ductile matrix fiber composites: Experiments and analysis. International journal of solids and structures 35, 1709–1722.

[51] Naya, F., Herráez, M., Lopes, C., González, C., der Veen, S.V., Pons, F., 2017. Computational micromechanics of fiber kinking in unidirectional frp under different environmental conditions. Composites Science and Technology 144, 26 – 35. URL: http://www.sciencedirect.com/science/article/pii/S0266353817300416, doi:https://doi.org/10.1016/j.compscitech.2017.03.014.

[52] Nguyen, M.H., Waas, A.M., 2022. Detailed experimental and numerical investigation of single-edge notched tensile cross-ply laminates. Composite Structures 279, 114731. URL: https://www.sciencedirect.com/science/article/pii/S0263822321011831,

doi:https://doi.org/10.1016/j.compstruct.2021.114731.

[53] Oskay, C., Fish, J., 2007. Eigendeformation-based reduced order homogenization for failure analysis of heterogeneous materials. Computer Methods in Applied Mechanics and Engineering 196, 1216–1243.

[54] Oskay, C., Pal, G., 2010. A multiscale failure model for analysis of thin heterogeneous plates. Int. J. Damage Mechanics 19, 575–611.

[55] Oskay, C., Su, Z., Kapusuzoglu, B., 2020. Discrete eigenseparation-based reduced order homogenization method for failure modeling of composite materials. Comput. Meth. Appl. Mech. Engrg. 359, 112656.

[56] Paluch, B., 1996. Analysis of geometric imperfections affecting the fibers in unidirectional composites. Journal of Composite Materials 30, 454–485. URL: https://doi.org/10.1177/002199839603000403, doi:10.1177/002199839603000403, arXiv:https://doi.org/10.1177/002199839603000403.

[57] Pinho, S., Darvizeh, R., Robinson, P., Schuecker, C., Camanho, P., 2012. Material and structural response of polymer-matrix fibre-reinforced composites. Journal of Composite Materials 46, 2313–2341. URL: https://doi.org/10.1177/0021998312454478, doi:10.1177/0021998312454478, arXiv:https://doi.org/10.1177/0021998312454478.

[58] Pinho, S., Robinson, P., Iannucci, L., 2006. Fracture toughness of the tensile and compressive fibre failure modes in laminated composites. Composites Science and Technology 66, 2069–2079. URL: https://www.sciencedirect.com/science/article/pii/S026635380600011X, doi:https://doi.org/10.1016/j.compscitech.2005.12.023.

[59] Poh, L.H., Sun, G., 2017. Localizing gradient damage model with decreasing interactions. International Journal for Numerical Methods in Engineering 110, 503–522.

[60] Prabhakar, P., Waas, A.M., 2013. Micromechanical modeling to determine the compressive strength and failure mode interaction of multidirectional laminates. Composites. Part A, Applied science and manufacturing 50, 11–21.

[61] R. Wisnom, M., Chang, F.K., 2000. Modelling of splitting and delamination in notched cross-ply laminates. Composites Science and Technology 60, 2849–2856. URL: https://www.sciencedirect.com/science/article/pii/S0266353800001706, doi:https://doi.org/10.1016/S0266-3538(00)00170-6.

[62] Ranatunga, V., Clay, S.B., 2013. Cohesive modeling of damage growth in z-pinned laminates under mode-i loading. Journal of Composite Materials 47, 3269–3283. URL: https://doi.org/10.1177/0021998312464078, doi:10.1177/0021998312464078, arXiv:https://doi.org/10.1177/0021998312464078.

[63] Schapery, R., 1995. Prediction of compressive strength and kink bands in composites using a work potential. International Journal of Solids and Structures 32, 739 – 765. URL: http://www.sciencedirect.com/science/article/pii/002076839400158S, doi:https://doi.org/10.1016/0020-7683(94)00158-S. time Dependent Problems in Mechanics.

[64] Shinohara, A.H., Sato, T., Saito, F., Tomioka, T., Arai, Y., 1993. A novel method for measuring direct compressive properties of carbon fibres using a micro-mechanical compression tester. Journal of materials science 28, 6611–6616.

[65] Skamniotis, C., Elliott, M., Charalambides, M., 2019. On modelling the constitutive and damage behaviour of highly non-linear bio-composites – mesh sensitivity of the viscoplastic-damage law computations. International journal of plasticity 114, 40–62.

[66] Soutis, C., Curtis, P.T., Fleck, N.A., 1993. Compressive failure of notched carbon fibre composites. Proceedings: Mathematical and Physical Sciences 440, 241–256. URL: http://www.jstor.org/stable/52233.

[67] Soutis, C., Fleck, N., Curtis, P., 1991. Hole-hole interaction in carbon fibre/epoxy laminates under uniaxial compression. Composites 22, 31–38.

[68] Sparks, P., Oskay, C., 2016. The method of failure paths for reduced-order computational homogenization. International Journal for Multiscale Computational Engineering 14, 515–534.

[69] Su, Z., Oskay, C., 2021. Mesh size objective fatigue damage propagation in laminated composites using the multiscale discrete damage theory. Computational Mechanics 67, 969–987. URL: https://doi.org/10.1007/s00466-021-01978-7, doi:10.1007/s00466-021-01978-7.

[70] Su, Z., Oskay, C., 2022. Modeling arbitrarily oriented and reorienting multiscale cracks in composite materials with adaptive multiscale discrete damage theory. Computational mechanics 70, 1041–1058.

[71] Suemasu, H., Takahashi, H., Ishikawa, T., 2006. On failure mechanisms of composite laminates with an open hole subjected to compressive load. Composites science and technology 66, 634–641.

[72] Sun, Q., Guo, H., Zhou, G., Meng, Z., Chen, Z., Kang, H., Keten, S., Su, X., 2018. Experimental and computational analysis of failure mechanisms in unidirectional carbon fiber reinforced polymer laminates under longitudinal compression loading. Composite Structures 203, 335–348. URL: https://www.sciencedirect.com/science/article/pii/S0263822318313278, doi:https://doi.org/10.1016/j.compstruct.2018.06.028.

[73] Tan, J., Deshpande, V., Fleck, N., 2015. Failure mechanisms of a notched cfrp laminate under multi-axial loading. Composites Part A: Applied Science and Manufacturing 77, 56–66. URL: https://www.sciencedirect.com/science/article/pii/S1359835X15002043, doi:https://doi.org/10.1016/j.compositesa.2015.06.005.

[74] Tan, J.L.Y., Deshpande, V.S., Fleck, N.A., 2016. Prediction of failure in notched carbon-fibre-reinforced-polymer laminates under multi-axial loading. Philosophical Transactions of the Royal Society A: Mathematical, Physical and Engineering Sciences 374, 20150273. URL: https://royalsocietypublishing.org/doi/abs/10.1098/rsta.2015.0273, doi:10.1098/rsta.2015.0273, arXiv:https://royalsocietypublishing.org/doi/pdf/10.1098/rsta.2015.0273.

[75] Turon, A., Camanho, P., Costa, J., Renart, J., 2010. Accurate simulation of delamination growth under mixed-mode loading using cohesive elements: Definition of interlaminar strengths and elastic stiffness. Composite structures 92, 1857–1864.

[76] Turon, A., Dávila, C., Camanho, P., Costa, J., 2007. An engineering solution for mesh size effects in the simulation of delamination using cohesive zone models. Engineering Fracture Mechanics 74, 1665–1682. URL: https://www.sciencedirect.com/science/article/pii/S0013794406003808, doi:https://doi.org/10.1016/j.engfracmech.2006.08.025.

[77] van der Meer, F., Oliver, C., Sluys, L., 2010. Computational analysis of progressive failure in a notched laminate including shear nonlinearity and fiber failure. Composites Science and Technology 70, 692–700. URL: https://www.sciencedirect.com/science/article/pii/S0266353810000059, doi:https://doi.org/10.1016/j.compscitech.2010.01.003.

[78] Vignoli, L.L., Savi, M.A., Pacheco, P.M., Kalamkarov, A.L., 2020. Micromechanical analysis of longitudinal and shear strength of composite laminae. Journal of Composite Materials 54, 4853–4873. URL: https://doi.org/10.1177/0021998320936343, doi:10.1177/0021998320936343, arXiv:https://doi.org/10.1177/0021998320936343.

[79] Vogler, T., Hsu, S.Y., Kyriakides, S., 2001. On the initiation and growth of kink bands in fiber composites. part ii: analysis. International Journal of Solids and Structures 38, 2653,2682.

[80] Vogler, T., Kyriakides, S., 1997. Initiation and axial propagation of kink bands in fiber composites. Acta Materialia 45, 2443 – 2454. URL: http://www.sciencedirect.com/science/article/pii/S1359645496003503, doi:https://doi.org/10.1016/S1359-6454(96)00350-3.

[81] Waas, A., Babcock, C., Knauss, W., 1990. An experimental study of compression failure of fibrous laminated composites in the presence of stress gradients. International journal of solids and structures 26, 1071–1098.

[82] Wang, Y., Burnett, T.L., Chai, Y., Soutis, C., Hogg, P.J., Withers, P.J., 2017. X-ray computed tomography study of kink bands in unidirectional composites. Composite Structures 160, 917 – 924. URL: http://www.sciencedirect.com/science/article/pii/S0263822316317159, doi:https://doi.org/10.1016/j.compstruct.2016.

10.124.

[83] Wilhelmsson, D., Talreja, R., Gutkin, R., Asp, L., 2019. Compressive strength assessment of fibre composites based on a defect severity model. Composites Science and Technology 181, 107685. URL: https://www.sciencedirect.com/science/article/pii/S0266353819303483, doi:https://doi.org/10.1016/j.compscitech.2019.107685.

[84] Wisnom, M., Hallett, S., Soutis, C., 2010. Scaling effects in notched composites. Journal of composite materials 44, 195–210.

[85] Yan, H., Oskay, C., Krishnan, A., Xu, L.R., 2010. Compression-after-impact response of woven fiber-reinforced composites. Composites Science and Technology 70, 2128 – 2136. URL: http://www.sciencedirect.com/science/article/pii/S0266353810003209, doi:https://doi.org/10.1016/j.compscitech.2010.08.012.

[86] Yerramalli, C., Waas, A., 2004. The effect of fiber diameter on the compressive strength of composites - a 3d finite element based study. Computer Modeling in Engineering and Sciences 6, 1–16.

[87] Zhou, S., Sun, Y., Chen, B., Tay, T.E., 2017. Progressive damage simulation of open-hole composite laminates under compression based on different failure criteria. Journal of Composite Materials 51, 1239–1251. URL: https://doi.org/10.1177/0021998316659776, doi:10.1177/0021998316659776, arXiv:https://doi.org/10.1177/0021998316659776.